

Smart Design of Cz-Ge Crystal Growth Furnace and Process

Natasha Dropka ^{1,*}, Xia Tang ¹, Gagan Kumar Chappa ¹ and Martin Holena ^{2,3}¹ Leibniz-Institut für Kristallzüchtung, Max-Born-Str. 2, 12489 Berlin, Germany² Leibniz Institute for Catalysis, Albert-Einstein-Str. 29A, 18069 Rostock, Germany³ Institute of Computer Science, Pod Vodárenskou Věží 2, 18207 Prague, Czech Republic* Correspondence: natascha.dropka@ikz-berlin.de

Abstract: The aim of this study was to evaluate the potential of the machine learning technique of decision trees to understand the relationships among furnace design, process parameters, crystal quality, and yield in the case of the Czochralski growth of germanium. The ultimate goal was to provide the range of optimal values of 13 input parameters and the ranking of their importance in relation to their impact on three output parameters relevant to process economy and crystal quality. Training data were provided by CFD modelling. The variety of data was ensured by the Design of Experiments method. The results showed that the process parameters, particularly the pulling rate, had a substantially greater impact on the crystal quality and yield than the design parameters of the furnace hot zone. Of the latter, only the crucible size, the axial position of the side heater, and the material properties of the radiation shield were relevant.

Keywords: Czochralski Ge growth; CFD training data; furnace design; process design; regression tree; correlation coefficient



Citation: Dropka, N.; Tang, X.; Chappa, G.K.; Holena, M. Smart Design of Cz-Ge Crystal Growth Furnace and Process. *Crystals* **2022**, *12*, 1764. <https://doi.org/10.3390/cryst12121764>

Academic Editor: Koichi Kakimoto

Received: 2 November 2022

Accepted: 29 November 2022

Published: 5 December 2022

Publisher's Note: MDPI stays neutral with regard to jurisdictional claims in published maps and institutional affiliations.



Copyright: © 2022 by the authors. Licensee MDPI, Basel, Switzerland. This article is an open access article distributed under the terms and conditions of the Creative Commons Attribution (CC BY) license (<https://creativecommons.org/licenses/by/4.0/>).

1. Introduction

Today, a century after its invention, Czochralski (Cz) growth is the dominant method in industry to produce large crystalline materials for modern electronic and photonic technologies [1–3]. Out of many parameters influencing the crystal quality and yield, the furnace design (e.g., geometry and the material properties of the hot zone parts) and process parameters (e.g., pulling and rotational rates, heating power, etc.) are essential. Their optimization has been the subject of extensive experimental and numerical research, especially in the case of the Cz growth of silicon (Cz-Si), e.g., [3–9], followed by germanium, gallium arsenide, and various oxides [10–13].

The furnace design studies focused mainly on optimizing the geometry of the radiation shield [4,11,14–18] and rarely on the position of the side heater [14], the geometry of the cooler [16], the flow guide [4], and the insulation materials [4,17]. Concerning process parameters, numerous papers were devoted to the study of the influences of the crystal and crucible rotational rates on the interface shape [9,19] and the limitations of the growth rates [20,21]. In magnetically driven Cz-Si growth, optimization of the magnetic parameters with respect to oxygen and carbon transport was a topic of numerous studies, e.g., [22–26]. The sensitivity of the Cz-Ge process dynamics to the pulling rate and heating power at the beginning and towards the end of the growth was investigated in [10].

Computational fluid dynamics (CFD) is a traditional numerical tool for solving the governing differential equations describing the transport phenomena during crystal growth that helped understand the crucial process steps and factors determining the crystal growth. The main challenge of this approach is the fact that CFD simulations are laborious, expensive, and time consuming without the ability to generalize.

One of the most exciting cutting-edge tools that entered the field of crystal growth over the last decade is machine learning (ML). It has a great potential to revolutionize

the optimization of the crystal growth processes and equipment, process control, and interpretability of the results in general [27].

Based on the added value achieved by combining ML and crystal growth research fields, we aimed to assess the potential of a selected interpretable ML technique for understanding the relationships among furnace design, process parameters, crystal quality, and yield in the case of Cz growth of germanium (Cz-Ge) to improve on the latter two. This study was motivated by the fact that Ge, a pioneering crystalline material in the history of electronics, is making a comeback as a next-generation semiconductor for applications in infrared optics, gamma-radiation detection, and photovoltaics [28–31]. The ultimate success in this endeavor depends on the quality and yield of the Ge crystals and their relationship to actual Si values [8].

One of the first attempts to develop the geometry of a bulk crystal growth furnace with ML support goes back to the work of Yu et al. [32], which was focused on the top-seeded solution growth of silicon carbide (TSSiC). The authors derived an artificial neural network (ANN) from 500 axisymmetric CFD simulations varying seven geometrical furnace parameters and optimizing the geometry using a genetic algorithm. Further ML studies were devoted to the applications of ANN and convolutional neural networks (CNN) to optimize process parameters in Cz-Si, Cz-YAG, DS-Si, and TSSiC growth [33–37].

The ANN and CNN are the most popular ML methods, characterized by a high accuracy of predictions but also a black-box nature, long computational times, and the demand for a large amount of training data. Our ML focus was on using the decision trees (DTs) method [38,39], which is suitable for applications with a small amount of data and high demands on the interpretability of the results (i.e., on understanding cause–effect relationships), which are common in crystal growth. Recently, we successfully applied regression and classification trees to study the influence of process parameters on interface deflection in VGF-GaAs growth [40].

In this study, Cz-Ge furnace and process design considerations included the hot zone geometry parameters, radiation shield material, heating power, rotation, and pulling rates.

Altogether, 13 input and 3 output parameters were considered. In total, 77 training data sets were provided by CFD modelling.

The pros and cons of the here proposed data-driven DT approach for Cz-Ge furnace and process design will be discussed and results compared with the common CFD and data-driven ANN approach.

2. Models and Methodology

2.1. Generation of Training Data by CFD Modelling

A sketch of the Cz-Ge furnace geometry with a definition of the main geometric and process parameters used in the simulations is given in Figure 1. The furnace was equipped with two graphite resistance heaters positioned on the side and bottom of the crucible. The quartz crucible was charged with 6.7 kg of Ge. The radiation shield was made of different materials and varied in length but had a constant slope. Its geometry guaranteed the visibility of the Ge triple point.

The transport phenomena taking place during the Cz-Ge growth were described by a common two-dimensional axisymmetric model. Governing equations for CFD modelling included equations of continuity, Navier-Stokes with the Boussinesq approximation, and energy Equations (1)–(5).

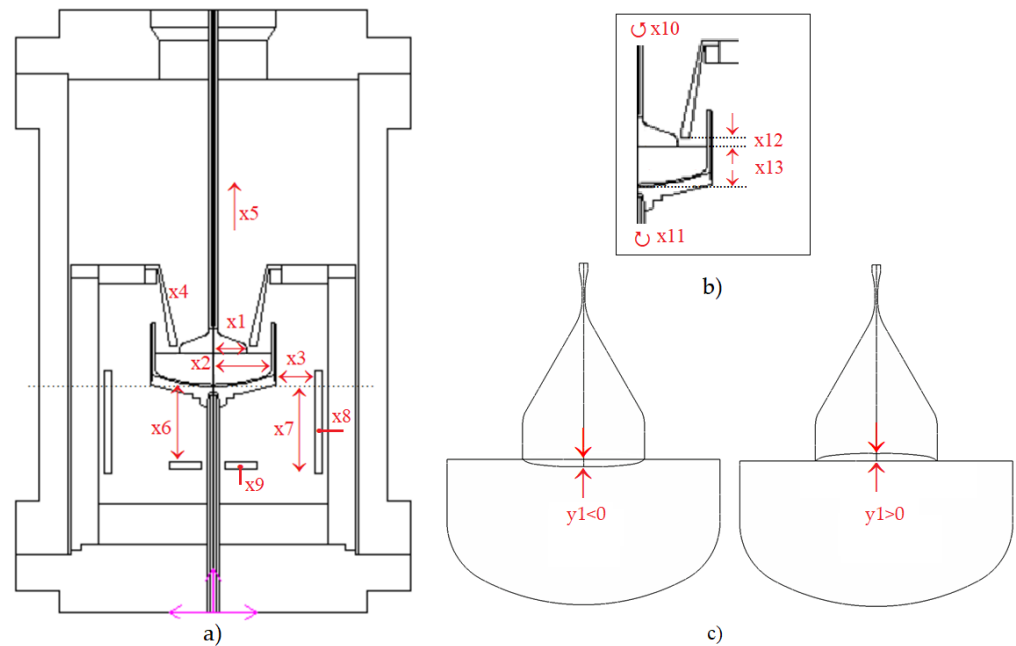


Figure 1. Furnace for Cz-Ge growth: (a,b) geometry with a definition of the main geometric and process parameters: x_1 , crystal radius; x_2 , crucible radius; x_3 , distance between crucible and side heater; x_4 , shield emissivity; x_5 , pulling rate; x_6 , distance between crucible and bottom heater; x_7 , axial displacement of side heater; x_8 , power of side heater; x_9 , power of bottom heater; x_{10} , crystal rotational rate; x_{11} , crucible rotational rate; x_{12} , distance from the radiation shield to the melt; x_{13} , melt height; (c) definition and a sign of interface deflection y_1 .

$$\frac{\partial \rho}{\partial t} + \nabla(\rho \cdot \vec{u}) = 0 \quad (1)$$

$$\frac{\partial(\rho \vec{u})}{\partial t} + (\vec{u} \cdot \nabla) \rho \vec{u} = -\nabla p + \nabla \tau + (\rho - \rho_0) \vec{g} \quad (2)$$

$$\frac{\partial(\rho c_p T)}{\partial t} + \nabla \cdot (\rho c_p \vec{u} T) = \nabla \cdot (\lambda \nabla T) \quad (3)$$

The Stefan and isothermal conditions must be fulfilled at the melt–crystal interface:

$$[(-\lambda_l \nabla T)_l + (\lambda_s \nabla T)_s] \cdot \vec{n}_{s,l} = \Delta H_s v \quad (4)$$

$$T = T_m \quad (5)$$

Details and theoretical backgrounds can be found elsewhere [41].

Due to the small size of the crucibles and crystals, Reynolds numbers were expected to be below the range typical for the turbulent flow. Against this background, melt convection was described by the laminar flow model.

The Ge material properties used in this study are given in Table 1. The crystals were grown in Ar atmosphere under atmospheric pressure. The CFD simulations were performed using the commercial code CGSim.

Table 1. Material properties of Ge melt and crystal.

Property Unit	T_m (K)	ρ (kg m^{-3})	μ (Pas)	λ ($\text{W m}^{-1}\text{K}^{-1}$)	c_p ($\text{J kg}^{-1}\text{K}^{-1}$)	α (K^{-1})	ε (-)	Pr (-)
Ge melt	1211	5670	7.42×10^{-4}	39	394	1.11×10^{-4}	0.5	0.008
Ge crystal		5323	-	17.3	404		0.5	

In order to obtain maximum information from a minimum number of CFD simulations, i.e., to cover relationships among 13 inputs and 3 outputs with good quality, a Design of Experiments (DoE) method [42] was used. If all input variables were varied at three levels, the theoretical number of CFD simulations (i.e., virtual experiments) based on a full factorial design would be $3^{13} = 1,594,323$, which is impossible to perform. In this study, we applied a D-optimal design for eight variables at three levels. However, nonsensical geometrical combinations and constrained process variables were discarded from DoE considerations.

For the generation of data sets for ML simulations, 77 combinations of seven geometric, one radiation shield material choice, and five crystal growth process parameters were used as input parameters for the CFD simulations. From the obtained axisymmetric CFD results, the interface deflection, crystal growth rate, and ratio of growth rate to the vertical temperature gradient (v/G) were extracted as output parameters for the ML training database. The interface deflection y_1 was selected as the main measure of the crystal quality due to its well-known correlation with the development of thermal stress-induced crystal dislocations [43].

The output v/G was included as an additional measure of crystal quality based on the following considerations. The so-called Voronkov criterion is one of the key parameters that defines the critical value of v/G for the growth of defect-free perfect silicon crystals for device processing [44]. For $v/G > 1.34 \times 10^{-3} \text{ cm}^2/\text{K min}$, the silicon crystal is vacancy rich, while for $v/G < 1.34 \times 10^{-3} \text{ cm}^2/\text{K min}$, the crystal is self-interstitial rich. Recent studies showed that application of the Voronkov criterion to a Cz-Ge single crystal is also possible when Ge is doped with Ga and Sb [45–48]. Otherwise, the vacancy is always the dominant intrinsic point defect for Cz-Ge [48]. Finally, we selected the crystal growth rate as a crucial parameter for the economics of the process.

The common optimization goal in industrial crystal growth is to find ranges of input parameters in which the economy and crystal quality criteria are met simultaneously. In our study, this multi-objective optimization goal corresponded to the cases where s/l interface was flat, the crystal growth rate was maximal, and the Voronkov criterion was satisfied. In other words, we looked for the minimum of the objective (fitness) function y_{123} that was defined as a combined normalized output:

$$y_{123} = \{|y_1|\} + \{-y_2\} + \{y_3 - 1.34 \times 10^{-3}\} \quad (6)$$

The data were pre-processed by normalization rescaling so that they ended up ranging between 0 and 1:

$$\{y_i\} = \frac{y_i - y_{i,min}}{y_{i,max} - y_{i,min}} \quad (7)$$

The fitness function y_{123} can also be defined in different ways, emphasizing the influence of certain outputs by adding weighting factors to Equation (6), as suggested in the literature [49]. In this study, we assumed that all outputs were equally important.

The interface deflection y_1 was measured at the melt symmetry axis with respect to the three-phase junction (melt/crystal/gas) and varied between detrimental concave ($y_1 > 0$) and favorable slightly convex ($y_1 < 0$), as shown in Figure 1c. Process parameters were selected from the typical range of values given in the literature [28], e.g., pulling rate, crystal, and crucible rotational rates were varied in the intervals 0.16–1.5 mm/min, 10–60 rpm and, –1 to –5 rpm, respectively. Although the radiation shield can be made from multiple materials in a stacked arrangement, for simplicity we used a single material shield made of either quartz, ceramics, or graphite. All material properties of the shield materials were taken into account in the CFD simulations. In the ML simulations, only the emissivity of the radiation shield was considered as an input parameter.

2.2. Correlation Coefficients

Because of its simplicity, we used correlation coefficients as a starting point for data analysis. The Pearson correlation coefficient r of any input x_i and output y_j pairs of random

variables is a measure of their linear dependence [50]. If each variable has N observations, then the Pearson correlation coefficient is defined as

$$r(x_i, y_j) = \frac{1}{N} \sum_{n=1}^N \left(\frac{x_{i,n} - \bar{x}_i}{\sigma_{x_i}} \right) \left(\frac{y_{j,n} - \bar{y}_j}{\sigma_{y_j}} \right) \quad (8)$$

where \bar{x}_i and σ_{x_i} are the empirical mean and standard deviation of x_i , respectively, and \bar{y}_j and σ_{y_j} are the empirical mean and standard deviation of y_j .

Two variables, x_i and y_j , are positively correlated ($r > 0$) if their values change in the same direction, negatively correlated ($r < 0$) if they change in the opposite direction, or may exhibit zero correlation ($r = 0$) if there is no relationship between the change of the variables. When interpreting the $r = 0$ results, the limitations of this simple approach must be taken into account, e.g., results may indicate zero correlation where non-linear dependences exist. Additionally, an observed correlation between the variables does not imply causation.

2.3. Regression Trees

The dependency between input and output parameters was modelled using regression trees (RTs), a non-linear regression model suitable for small data sets and high interpretability requirements. Regression trees are a type of decision trees where the output variables are real numbers [39].

The method enables us to analyze how the combination of input variables affects the outputs and to predict them individually. It has a tree structure, starting from the topmost root node with the initial data set, undergoing recursive binary splitting down in each node until the terminal node is reached that either is in a given maximal depth or has at most a given minimum size. The nodes represent the input variables: each branch is a decision and both nodes below a branch are the more homogeneous subsets of the data set above the branch. The splits are based on the sum of squared errors (SSE) with respect to the means of the y_j in the two subsets, S_1 and S_2 , forming the split

$$SSE(S_1, S_2) = \sum_{x_i \in S_1} \left(y_i - \frac{1}{|S_1|} \sum_{x_i \in S_1} y_i \right)^2 + \sum_{x_i \in S_2} \left(y_i - \frac{1}{|S_2|} \sum_{x_i \in S_2} y_i \right)^2 \quad (9)$$

From all possible splits of the data set S above the branch, a split S_1^*, S_2^* was chosen that led to the minimal sum of squared errors.

$$SSE(S_1^*, S_2^*) = \min\{SSE(S_1, S_2); (S_1, S_2) \text{ is some split of } S\} \quad (10)$$

The fitted model can be used to predict y_j values as a function of x_i variables. In this study, the maximum tree depth was set at 10.

From the regression trees for the crystal growth rate, the interface deflection, and the v/G ratio, the importance of each input variable (also known as feature importance) was also derived. Feature importance is the sum of the mean square error (RMSE) reductions across all those interior nodes in which this input variable resulted in the highest RMSE reduction in the node.

3. Results and Discussion

3.1. CFD Modelling

The CFD results provided 77 data sets in the form of 16-dimensional vectors, each with 13 input and 3 output parameters. All data are presented in parallel coordinates in Figure 2. Each line in the diagram corresponds to one data tuple ($x_1 \dots x_{13}, y_1 \dots y_3$). The generated database was used for ML training and analysis. The line color in Figure 2a,b matches the value of the interface deflection y_1 and v/G ratio y_3 , respectively. In both cases, the visual inspection of the results indicated the strong influence of the pulling rate x_5 , as known from experimental investigations, i.e., the higher the pulling rate x_5 , the lower the crystal quality due to higher concavity of the interface ($y_1 > 0$) and the v/G value (y_3). Similarly,

as the crystal radius x_1 increases, so does the interface concavity y_1 , which is the well-known challenge of upscaling.

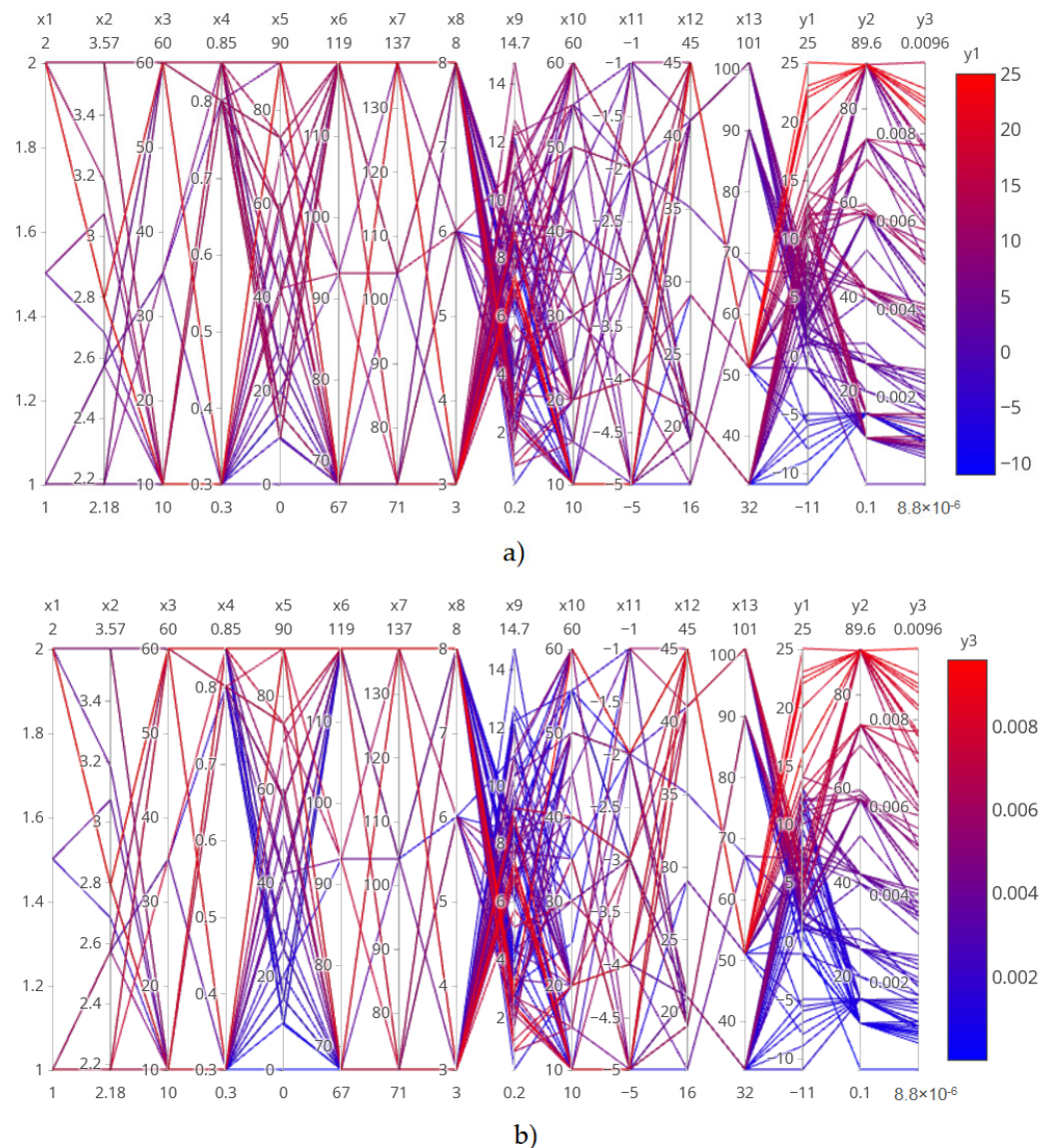


Figure 2. All CFD results derived from 77 crystal growth recipes shown in parallel coordinate system for inputs x_1 – x_{13} and outputs y_1 – y_3 . The line color matches the value of: (a) the interface deflection y_1 and (b) $v/G = y_3$. The database was used for ML analysis.

Examples of axisymmetric quasi-steady state CFD simulation results for various furnace designs and growth recipes in a form of temperature and melt velocity distributions in the Cz-furnace are shown in Figure 3. The melt flow patterns reflected the typical superposition of buoyancy-driven convection and forced convection due to crystal and crucible rotation. Interface deflection varied among concave (Figure 3a), convex (Figure 3b), and nearly flat (Figure 3c) depending on the used growth recipe, hot zone design, and materials' allocation.

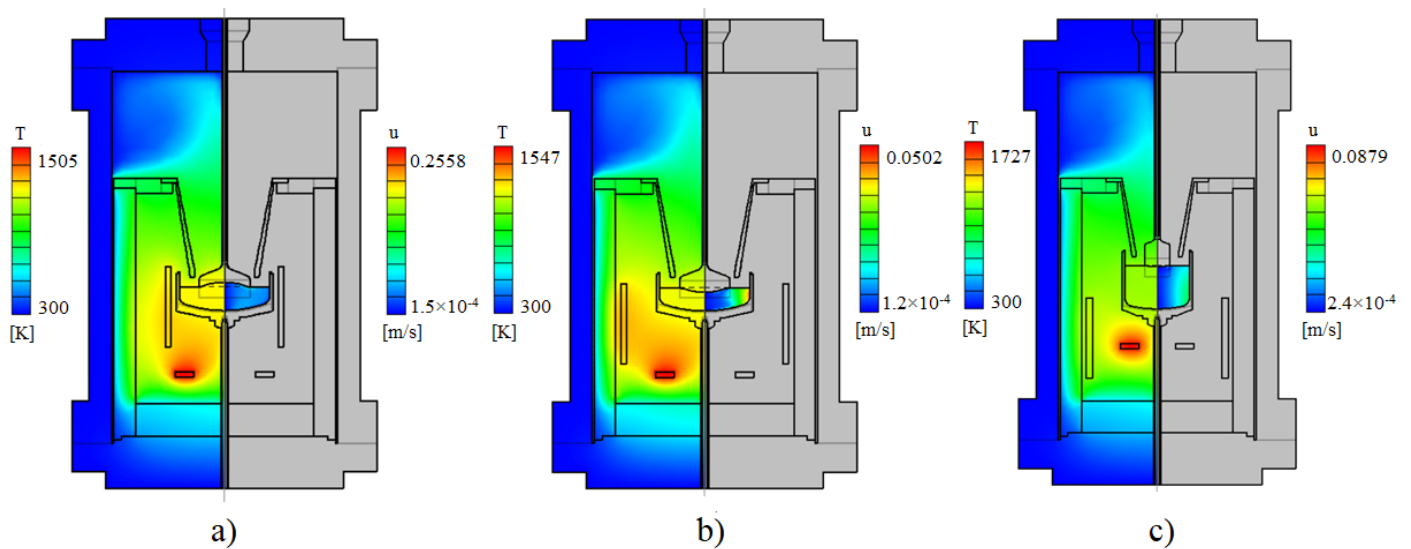


Figure 3. Examples of CFD results for the temperature T in the furnace and the melt velocity u for various furnace designs and growth recipes. The results correspond to the following inputs x_1 – x_{13} : (a) 2; 3.574803; 10; 0.8; 58; 119; 71; 6; 7.6; 50; –2; 21; 32; (b) 2; 3.574803; 60; 0.3; 15; 119; 104; 8; 8.1; 10; –5; 21; 32; (c) 1; 2.574803; 60; 0.3; 10; 67; 137; 3; 9.2; 35; –5; 19; 90.

3.2. Data Mining and Machine Learning

The resulting values for the correlation coefficients for all inputs and outputs are shown in Figure 4 and Table A1.

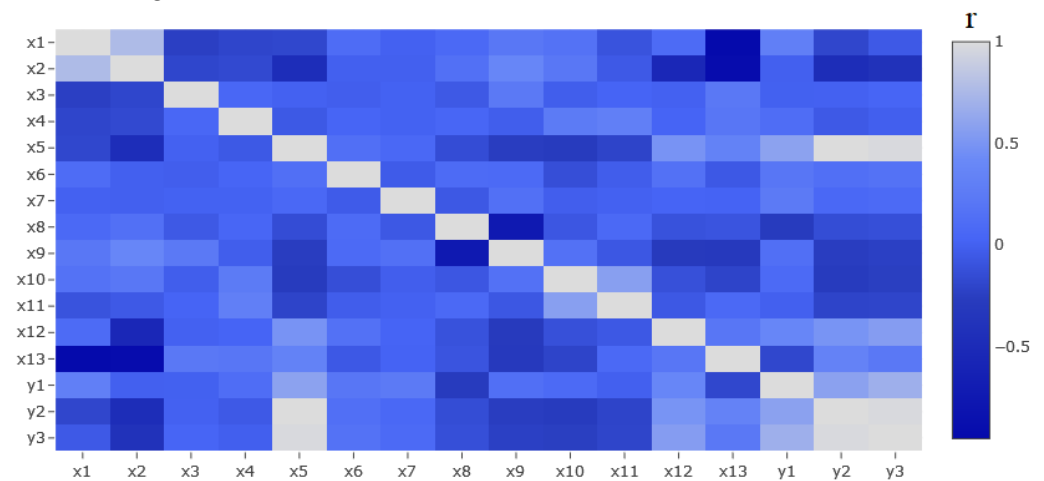


Figure 4. Correlation coefficients r for all 77 data tuples shown as colored correlation plots. The corresponding numerical matrix is given in Table A1 in Appendix A.

The strongest linear correlation between interface deflection y_1 and one of the inputs was observed for pulling rate x_5 . Their correlation coefficient with value $r_{x_5, y_1} = 0.5877$ showed medium-strong positive correlation. This result is in agreement with the experimental observations that higher pulling rates generate more latent heat at the crystallization front and finally more concave interface. Please note that in this study convex interface deflection had a negative value ($y_1 < 0$) and a negative correlation was beneficial for the crystal quality. The strongest linear correlation between the growth rate y_2 and one of the inputs was again observed for the pulling rate x_5 , with a correlation coefficient of $r_{x_5, y_2} = 0.9999$. This finding is supported by crystal growth experiments and is one of the reasons why pulling rates and crystal growth rates are often treated as interchangeable terms. Finally, the strongest positive linear correlation between y_3 and other inputs was observed for x_5 (the pulling rate) and for x_{12} (distance from the radiation shield to the melt,

i.e., melt gap) with correlation coefficients of $r_{x_5,y_3} = 0.9781$ and $r_{x_{12},y_3} = 0.5517$, respectively. Similar results were reported in the literature for Cz-Si growth [5,7]. Additionally, the strong linear correlations were observed between inputs x_1 (crystal radius) and x_2 (crucible radius) from one side and x_{13} (melt height) from the other side. The large negative values $r_{x_1,x_{13}} = -0.9512$ and $r_{x_2,x_{13}} = -0.9213$ were a consequence of the assumption of constant Ge loading in this study.

The correlation coefficients provided the first simple estimate of the linear dependencies between the examined parameters. However, many dependencies in crystal growth are strongly non-linear and need to be further investigated. A viable solution for studying complex relationships in small data sets is provided by regression trees.

The regression trees for outputs y_1 – y_3 , $y_{1,2,3}$ are given in Figures 5–8 and summarized in Tables 2–5. The value in the root node at the top of each regression tree represents the mean of the examined output y_i in all the data in the database. The values in interior nodes and leaf nodes correspond to the mean value of output y_i in the set of data remaining over the node after the last splitting. The root mean square error (RMSE) for each split is given in Table A2 in appendix. The path from the root to the leaf at the bottom of the tree indicates the influence of a given input x_i on the output y_i under study, with the highest relevance at the top and lowest at the bottom.

The resulting RT for interface deflection y_1 reveals x_5 , followed by x_{10} and x_9 as the most decisive inputs for the favorable flat or slightly convex interface shape (interface deflection $y_1 \leq 0$, the nodes marked white in the tree graph in Figure 5). Their importance decreased in the order mentioned above. The most decisive input was the pulling rate x_5 , which had a deteriorating effect on the interface deflection, i.e., x_5 should be below 22.8 mm/min to strongly reduce y_1 from average $y_1 = 5.84$ mm to average $y_1 = 1.4$ mm. All decisive inputs and ranges of their optimal values that assured the Cz-Ge growth with nearly flat s/l interface, derived from RT analysis, are given in Table 2. From these results, it was also possible to derive the relative feature importance for y_1 , as shown in Figure 9a. Again, the most important input concerning its influence on interface deflection had a pulling rate x_5 (32.7%), followed by crystal rotational rate x_{10} (30.91%), crystal radius x_1 (22.31%), and power of bottom heater x_9 (10.34%). The importance of the input x_1 was high but not conducive to interface flattening. Therefore, x_1 did not appear in the branches marked in white, leading to the optimal value of the interface deflection in Figure 5.

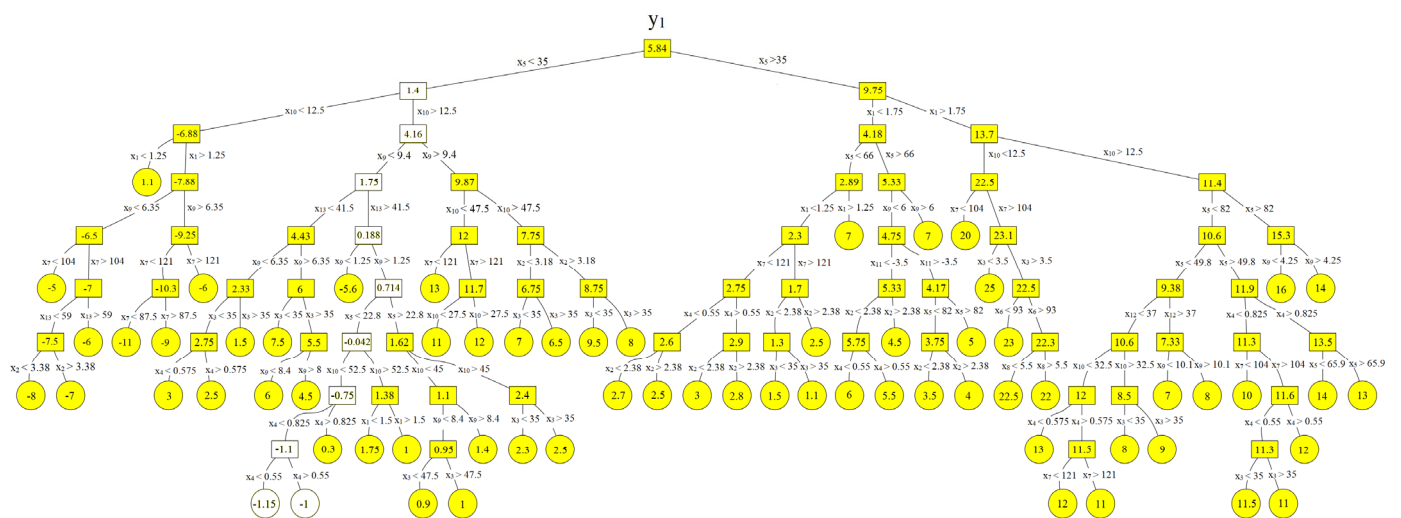


Figure 5. Regression tree analyzing the dependence of the solid–liquid interface deflection y_1 (mm) on the furnace design and process parameters x_1 – x_{13} . The white-marked branches where leaf nodes have a mean deflection $y_1 \leq 0$ mm, i.e., a slightly convex shape of s/l interface, are favorable. The RMSE for each split is given in Table A2 in Appendix A.

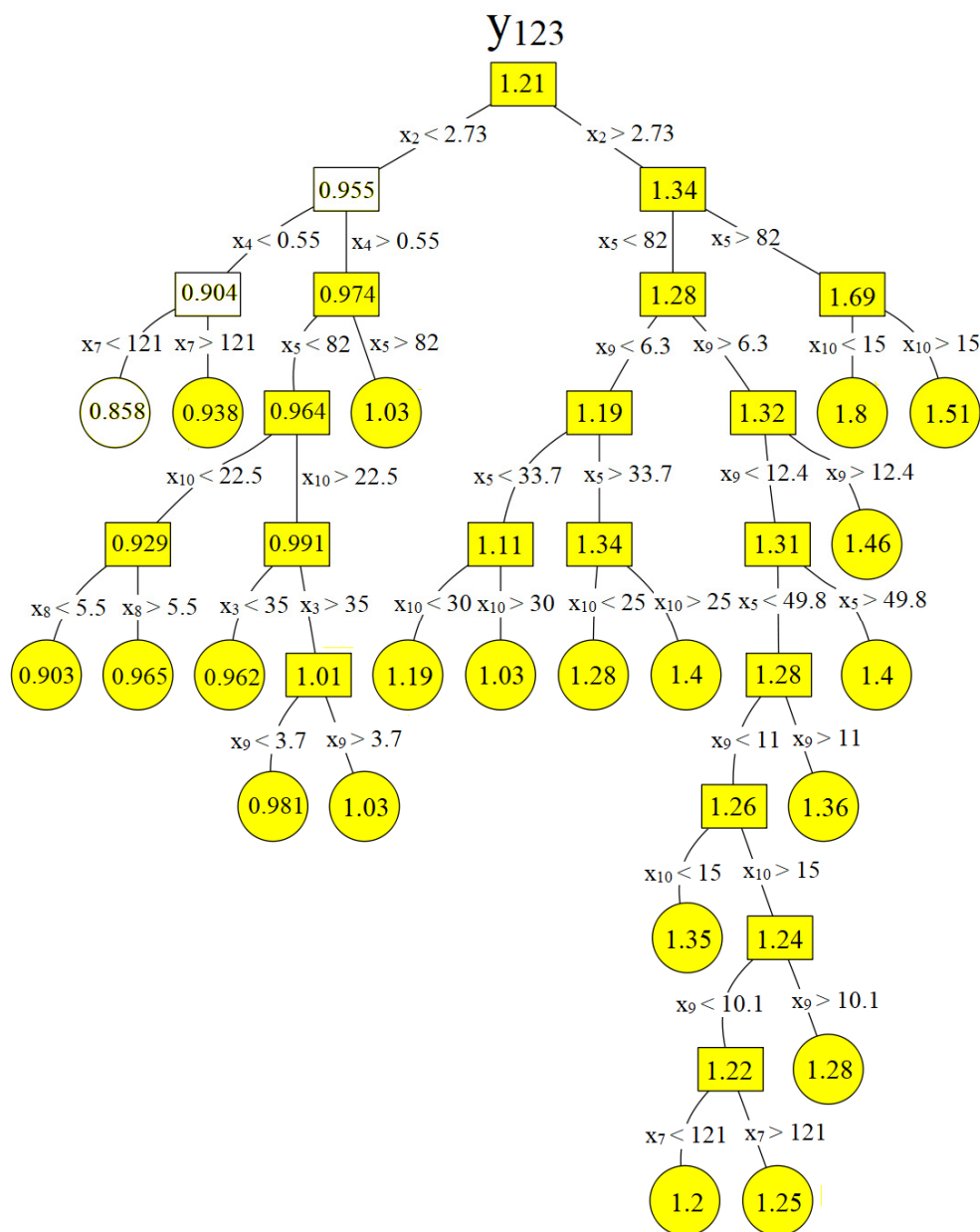


Figure 8. Regression tree analyzing the dependence of the normalized combined output y_{123} on the furnace design and process parameters x_1 – x_{13} . In the case of doped Ge, the branch where leaf node has a minimal mean value $y_{123} \sim 0.858$ (-) is favorable. The RMSE for each split is given in Table A2 in Appendix A.

Table 2. The most decisive inputs and their optimal values for the Cz-Ge growth with flat or slightly convex s/l interface ($y_1 \leq 0$ mm), derived from RT analysis. The data ranges correspond to the white nodes in Figure 5.

Mean	Decisive Inputs				
y_1	x_4	x_5	x_9	x_{10}	x_{13}
-1	$0.55 < * < 0.825$	< 22.8	$1.25 < * < 9.4$	$12.5 < * < 52.5$	> 41.5
-1.15	< 0.55	< 22.8	$1.25 < * < 9.4$	$12.5 < * < 52.5$	> 41.5

Table 3. The most decisive inputs and their optimal values for the Cz-Ge growth with high growth rate y_2 , derived from RT analysis. The data ranges correspond to the white nodes in Figure 6.

Mean	Decisive Inputs		
y_2	x_4	x_5	x_7
89.6	>0.575	>82	<104
89.2	<0.575	>82	<104

Table 4. The most decisive inputs and their optimal values for the favorable y_3 ($\text{cm}^2/\text{K min}$) value corresponding to the Voronkov criteria, derived from RT analysis. The data ranges correspond to the white nodes in Figure 7.

Mean	Decisive Inputs				
y_3	x_2	x_5	x_9	x_{10}	x_{11}
0.00126	>3.18	$12.5 < * < 22.8$	<11.3	>15	<-2.5
0.00141	<3.18	$12.5 < * < 22.8$	<11.3	>15	<-2.5

Table 5. The most decisive inputs and their optimal values for the favorable y_{123} value, derived from RT analysis. The data ranges correspond to the white nodes in Figure 8.

Mean	Decisive Inputs		
y_{123}	x_2	x_4	x_7
0.858	>2.73	>0.55	>121

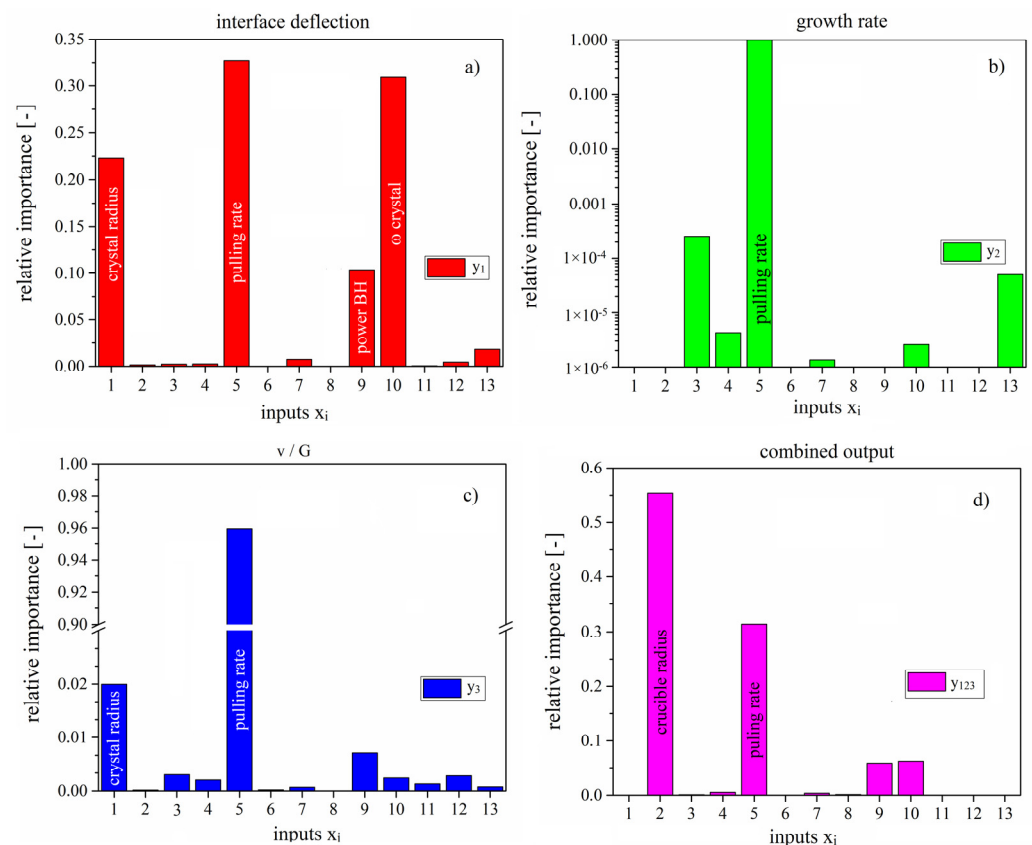


Figure 9. Relative importance of the inputs for: (a) interface deflection y_1 , (b) crystal growth rate y_2 , (c) ratio of growth rate and axial temperature gradient in the crystal y_3 , and (d) combined normalized output y_{123} .

The resulting RT for the crystal growth rate y_2 gave the pulling rate x_5 , followed by the position of the side heater x_7 and the emissivity of the radiation shield x_4 as the most decisive inputs for the favorable crystal yield (i.e., the maximum value of y_2 , corresponding to the nodes in the tree graph in Figure 6 marked white). Their importance decreased in the order mentioned above. All decisive inputs for y_2 and ranges of their optimal values are given in Table 3. The relative inputs' importance for y_2 is shown in Figure 9b. The pulling rate x_5 with 99.96% influenced the growth rate, followed by 0.025% and 0.005% relative influence of x_3 and x_{13} , respectively. These ML/RT results confirmed the general assumption in Cz crystal growth practice of the equivalence between the growth rate and the pulling rate. In view of this, ML results can serve as the last trusted criterion to explain various assumptions, free from human errors.

The resulting RT for the output y_3 (ratio of growth rate and axial temperature gradient in the crystal) is shown in Figure 7. The most decisive inputs for the favorable value y_3 according to the Voronkov criteria were x_5 , x_{10} , x_9 , x_{11} , and x_2 (the nodes in Figure 7 are marked in white). As already mentioned, the Voronkov criteria for defect-free Cz-Si crystals can only be applied to Cz-Ge if the crystal is doped with Ga and Sb. The optimal values of the most critical inputs are given in Table 4, and the relative importance of all inputs is shown in Figure 9c. The pulling rate x_5 with 95.96% influenced the y_3 , followed by 1.99% and 0.71% relative influence of x_1 and x_9 , respectively.

The RT for the combined output y_{123} is given in Figure 8. The favorable values of the input parameters correspond to the minimal leaf mean value of the objective function $y_{123} = 0.878$. The most decisive inputs for the favorable mean value y_{123} were x_2 , x_4 , and x_7 (the white nodes in Figure 8). Their related data ranges are given in Table 5, and the relative importance of all inputs is shown in Figure 9d.

In summary, our data-driven study based on the decision trees and synthetic training data revealed the key furnace design and process parameters, their importance, and the ranges of their values for achieving high-quality, high-yield Cz-Ge crystals. Interestingly, the process parameters, especially the pulling rate, had a substantially larger impact on all singular outputs than the furnace hot-zone design parameters. Among the latter, only the crucible size, the axial position of the side heater, and the material properties of the radiation shield were relevant.

In the case of a combined output y_{123} with equal contribution of each singular output y_1 – y_3 , the obtained results were different, i.e., the furnace design parameters such as crucible size, the axial position of the side heater, and the material properties of the radiation shield were more important than the pulling rate. However, the last result strongly depended on the definition of y_{123} (i.e., on the weighting of contributions of individual outputs and on the justification of consideration of y_3) and could not be generalized.

4. Conclusions

The decision trees are an excellent choice for studying Cz-Ge crystal growth if one needs methods with short training times and acceptable prediction accuracy based on low-volume data (77 in this study) that are able to provide guidelines for understanding the influences of the furnace design and the process parameters on the process economy and crystal quality. The decision trees also provide ranges of 13 input parameters (7 geometric, 1 radiation shield material choice, and 5 crystal growth process parameters) where optimal values of three targeted output variables (s/l interface deflection, growth rate, and v/G ratio) can be found.

Compared to the standard approach to furnace and process development based solely on CFD simulations, e.g., [4,5], characterized by accurate but slow predictions with no ability to generalize and more novel deep learning methods that require a large amount of training data to be accurate and have a black-box nature, e.g., [32], decision trees offer high interpretability with acceptable accuracy at low cost. Against this background, decision trees are a recommendable steppingstone in the development of new processes

and equipment for various grown materials and growth techniques before applying high-prediction accuracy methods such as ANN.

Author Contributions: Conceptualization, N.D. and M.H.; methodology, N.D. and M.H.; software, M.H. and N.D.; investigation, M.H., N.D. and X.T.; data generation, X.T., G.K.C. and N.D.; writing—original draft preparation, N.D.; writing—review and editing, N.D., M.H., G.K.C. and X.T.; funding acquisition, N.D. and M.H. All authors have read and agreed to the published version of the manuscript.

Funding: The research was partly funded by the German Research Foundation, project number 467401796.

Data Availability Statement: Data available in the IKZ repository.

Acknowledgments: Proofreading of the article by Kevin-Peter Gradwohl is gratefully acknowledged.

Conflicts of Interest: The authors declare no conflict of interest.

Nomenclature

c_p	heat capacity (J/kg/K)
g	gravity constant (m/s^2)
ΔH	latent heat (J/kg)
u	velocity (m/s)
v	growth rate (m/s)
T	temperature (K)
t	time (s)
x_1	crystal radius (inch)
x_2	crucible radius (inch)
x_3	distance between crucible and side heater (mm)
x_4	emissivity of the radiation shield (-)
x_5	pulling rate (mm/h)
x_6	distance between crucible and bottom heater (mm)
x_7	axial displacement of side heater (mm)
x_8	power of side heater (kW)
x_9	power of bottom heater (kW)
x_{10}	crystal rotational rate (rpm)
x_{11}	crucible rotational rate (rpm)
x_{12}	distance from the radiation shield to the melt (mm)
x_{13}	melt height (mm)
y_1	interface deflection (mm)
y_2	growth rate (mm/h)
y_3	ratio of the growth rate and axial temperature gradient in crystal v/G ($cm^2/K \text{ min}$)
y_{123}	combined output (-)
Symbols	
α	volume expansion coefficient (1/K)
λ	heat conductivity (W/m/K)
ρ	density (kg/m^3)
τ	stress tensor (Pa)
$ $	absolute value
$\{ \}$	normalized value
Subscripts	
l	liquid
m	melting
s	solid

Appendix A

Table A1. Correlation coefficients for input and output variables x_1 – x_{13} , y_1 – y_3 .

	x_1	x_2	x_3	x_4	x_5	x_6	x_7	x_8	x_9	x_{10}	x_{11}	x_{12}	x_{13}
x_1	1.00	0.77	−0.24	−0.20	−0.19	0.10	0.00	0.07	0.21	0.16	−0.10	0.09	−0.95
x_2	0.77	1.00	−0.20	−0.17	−0.48	−0.01	−0.01	0.14	0.38	0.21	−0.05	−0.55	−0.92
x_3	−0.24	−0.20	1.00	0.05	0.00	−0.02	0.01	−0.06	0.23	−0.02	0.02	0.00	0.22
x_4	−0.20	−0.17	0.05	1.00	−0.06	0.03	0.01	0.04	−0.02	0.25	0.30	0.02	0.20
x_5	−0.19	−0.48	0.00	−0.06	1.00	0.13	0.07	−0.15	−0.26	−0.28	−0.21	0.49	0.33
x_6	0.10	−0.01	−0.02	0.03	0.13	1.00	−0.04	0.09	0.08	−0.14	−0.03	0.15	−0.06
x_7	0.00	−0.01	0.01	0.01	0.07	−0.04	1.00	−0.07	0.15	−0.02	0.00	0.02	0.02
x_8	0.07	0.14	−0.06	0.04	−0.15	0.09	−0.07	1.00	−0.75	−0.08	0.07	−0.11	−0.09
x_9	0.21	0.38	0.23	−0.02	−0.26	0.08	0.15	−0.75	1.00	0.15	−0.07	−0.29	−0.31
x_{10}	0.16	0.21	−0.02	0.25	−0.28	−0.14	−0.02	−0.08	0.15	1.00	0.57	−0.13	−0.21
x_{11}	−0.10	−0.05	0.02	0.30	−0.21	−0.03	0.00	0.07	−0.07	0.57	1.00	−0.07	0.07
x_{12}	0.09	−0.55	0.00	0.02	0.49	0.15	0.02	−0.11	−0.29	−0.13	−0.07	1.00	0.20
x_{13}	−0.95	−0.92	0.22	0.20	0.33	−0.06	0.02	−0.09	−0.31	−0.21	0.07	0.20	1.00
y_1	0.30	−0.01	0.00	0.12	0.59	0.20	0.25	−0.29	0.14	0.09	−0.01	0.38	−0.19
y_2	−0.19	−0.48	0.00	−0.06	1.00	0.13	0.07	−0.15	−0.26	−0.28	−0.21	0.49	0.34
y_3	−0.06	−0.41	0.03	−0.01	0.98	0.16	0.08	−0.13	−0.24	−0.25	−0.20	0.55	0.22

Table A2. The RMSE values for each split in regression trees for y_1 , y_2 , y_3 and y_{123} . The nodes are numbered from the top of the tree down and from the left to the right at each tree depth.

Node	y_1 RMSE	y_2 RMSE	y_3 RMSE	y_{123} RMSE	Node	y_1 RMSE	y_3 RMSE	Node	y_1 RMSE	y_3 RMSE
1	7.59×10^{00}	2.87×10^{01}	2.63×10^{-03}	2.52×10^{-01}	42	1.80×10^{-01}	1.09×10^{-04}	83	0.00×10^{00}	0.00×10^{00}
2	6.47×10^{00}	1.18×10^{01}	1.11×10^{-03}	6.62×10^{-02}	43	5.89×10^{-01}	0.00×10^{00}	84	4.44×10^{-16}	0.00×10^{00}
3	6.24×10^{00}	1.44×10^{01}	1.63×10^{-03}	2.08×10^{-01}	44	6.24×10^{-01}	9.88×10^{-05}	85	0.00×10^{00}	0.00×10^{00}
4	3.47×10^{00}	3.91×10^{00}	5.92×10^{-04}	6.26×10^{-02}	45	6.24×10^{-01}	4.34×10^{-19}	86	8.88×10^{-16}	0.00×10^{00}
5	4.62×10^{00}	7.39×10^{00}	2.64×10^{-04}	5.67×10^{-02}	46	3.55×10^{-15}	1.81×10^{-04}	87	0.00×10^{00}	0.00×10^{00}
6	1.87×10^{00}	7.72×10^{00}	1.06×10^{-03}	1.37×10^{-01}	47	4.08×10^{-01}	8.67×10^{-19}	88	6.10×10^{-01}	0.00×10^{00}
7	5.15×10^{00}	1.39×10^{-01}	8.89×10^{-04}	1.68×10^{-01}	48	2.18×10^{00}	6.78×10^{-05}	89	3.75×10^{-01}	6.90×10^{-05}
8	0.00×10^{00}	2.82×10^{00}	3.58×10^{-04}	5.55×10^{-02}	49	1.17×10^{00}	0.00×10^{00}	90	2.16×10^{-01}	2.06×10^{-05}
9	2.15×10^{00}	1.58×10^{00}	2.65×10^{-04}	4.27×10^{-02}	50	0.00×10^{00}	0.00×10^{00}	91	1.00×10^{-01}	5.37×10^{-05}
10	2.92×10^{00}	1.41×10^{00}	2.23×10^{-04}	4.97×10^{-02}	51	0.00×10^{00}	2.49×10^{-04}	92	0.00×10^{00}	6.60×10^{-05}
11	2.33×10^{00}	9.17×10^{-01}	1.95×10^{-04}	6.00×10^{-02}	52	5.00×10^{-01}	8.38×10^{-05}	93	0.00×10^{00}	1.78×10^{-05}
12	1.67×10^{00}	2.37×10^{00}	6.49×10^{-04}	1.41×10^{-01}	53	8.88×10^{-16}	5.03×10^{-05}	94	4.44×10^{-16}	3.45×10^{-05}
13	1.15×10^{00}	1.61×10^{00}	8.15×10^{-04}	1.08×10^{-01}	54	0.00×10^{00}	2.96×10^{-04}	95	0.00×10^{00}	2.64×10^{-05}
14	1.61×10^{00}	2.05×10^{-01}	5.17×10^{-04}	7.30×10^{-02}	55	0.00×10^{00}	1.75×10^{-04}	96	2.22×10^{-16}	7.01×10^{-05}
15	2.64×10^{00}	0.00×10^{00}	5.49×10^{-04}	1.19×10^{-01}	56	2.50×10^{-01}	1.19×10^{-04}	97	0.00×10^{00}	7.62×10^{-05}
16	1.12×10^{00}	0.00×10^{00}	2.94×10^{-04}	3.60×10^{-02}	57	2.22×10^{-16}	0.00×10^{00}	98	8.88×10^{-16}	0.00×10^{00}
17	2.05×10^{00}	0.00×10^{00}	2.64×10^{-04}	4.16×10^{-02}	58	0.00×10^{00}	9.60×10^{-05}	99	0.00×10^{00}	3.40×10^{-06}
18	2.03×10^{00}	1.12×10^{-01}	1.55×10^{-04}	8.84×10^{-02}	59	7.07×10^{-01}	9.02×10^{-05}	100	0.00×10^{00}	0.00×10^{00}

Table A2. Cont.

Node	Y1 RMSE	Y2 RMSE	Y3 RMSE	Y123 RMSE	Node	Y1 RMSE	Y3 RMSE	Node	Y1 RMSE	Y3 RMSE
19	2.12×10^{00}	0.00×10^{00}	1.14×10^{-04}	7.98×10^{-02}	60	1.14×10^{00}	0.00×10^{00}	101	0.00×10^{00}	1.65×10^{-05}
20	7.07×10^{-01}	6.28×10^{-01}	2.68×10^{-05}	1.03×10^{-01}	61	6.62×10^{-01}	4.33×10^{-05}	102	0.00×10^{00}	2.68×10^{-05}
21	1.15×10^{00}	3.55×10^{-15}	4.34×10^{-19}	1.55×10^{-02}	62	0.00×10^{00}	1.32×10^{-04}	103	0.00×10^{00}	8.12×10^{-05}
22	6.61×10^{-01}	7.11×10^{-15}	1.54×10^{-04}	2.46×10^{-02}	63	1.78×10^{-15}	1.50×10^{-05}	104	8.16×10^{-01}	6.55×10^{-05}
23	0.00×10^{00}	0.00×10^{00}	0.00×10^{00}	6.93×10^{-03}	64	0.00×10^{00}	0.00×10^{00}	105	5.00×10^{-01}	0.00×10^{00}
24	8.54×10^{-01}	0.00×10^{00}	3.62×10^{-04}	4.81×10^{-02}	65	0.00×10^{00}	0.00×10^{00}	106	0.00×10^{00}	0.00×10^{00}
25	0.00×10^{00}	6.20×10^{-01}	2.73×10^{-04}	2.87×10^{-02}	66	0.00×10^{00}	0.00×10^{00}	107	0.00×10^{00}	0.00×10^{00}
26	0.00×10^{00}	0.00×10^{00}	1.72×10^{-04}	4.37×10^{-02}	67	0.00×10^{00}	0.00×10^{00}	108	0.00×10^{00}	0.00×10^{00}
27	1.14×10^{00}	1.26×10^{-01}	5.86×10^{-04}	2.81×10^{-02}	68	1.00×10^{-01}	0.00×10^{00}	109	4.90×10^{-01}	0.00×10^{00}
28	2.15×10^{00}	9.43×10^{-02}	0.00×10^{00}	6.82×10^{-02}	69	1.00×10^{-01}	4.90×10^{-05}	110	0.00×10^{00}	3.06×10^{-05}
29	9.43×10^{-01}	0.00×10^{00}	2.81×10^{-04}	2.34×10^{-02}	70	2.00×10^{-01}	8.04×10^{-05}	111	0.00×10^{00}	0.00×10^{00}
30	0.00×10^{00}	4.33×10^{-02}	3.62×10^{-04}	9.16×10^{-02}	71	0.00×10^{00}	4.34×10^{-19}	112	8.16×10^{-02}	3.86×10^{-05}
31	8.16×10^{-01}	7.45×10^{-02}	3.39×10^{-04}	8.80×10^{-02}	72	2.50×10^{-01}	2.02×10^{-06}	113	0.00×10^{00}	1.08×10^{-19}
32	9.43×10^{-01}	7.11×10^{-15}	0.00×10^{00}	1.36×10^{-02}	73	0.00×10^{00}	5.84×10^{-06}	114	0.00×10^{00}	0.00×10^{00}
33	8.88×10^{-16}	0.00×10^{00}	1.60×10^{-04}	1.72×10^{-02}	74	2.50×10^{-01}	8.67×10^{-19}	115	0.00×10^{00}	0.00×10^{00}
34	6.24×10^{-01}	1.36×10^{-01}	5.59×10^{-05}	6.25×10^{-02}	75	0.00×10^{00}	1.39×10^{-04}	116	5.00×10^{-02}	0.00×10^{00}
35	1.06×10^{00}	5.00×10^{-01}	1.19×10^{-04}	1.32×10^{-01}	76	3.55×10^{-15}	0.00×10^{00}	117	0.00×10^{00}	4.82×10^{-06}
36	0.00×10^{00}	0.00×10^{00}	5.36×10^{-05}	3.71×10^{-02}	77	2.50×10^{-01}	8.67×10^{-19}	118	0.00×10^{00}	0.00×10^{00}
37	1.26×10^{00}	8.66×10^{-02}	5.60×10^{-05}	4.67×10^{-02}	78	1.85×10^{00}	0.00×10^{00}	119	0.00×10^{00}	1.43×10^{-05}
38	0.00×10^{00}	0.00×10^{00}	8.66×10^{-05}	3.77×10^{-02}	79	4.71×10^{-01}	0.00×10^{00}	120	0.00×10^{00}	0.00×10^{00}
39	4.71×10^{-01}	7.28×10^{-02}	0.00×10^{00}	4.32×10^{-02}	80	7.45×10^{-01}	8.67×10^{-19}	121	5.00×10^{-01}	0.00×10^{00}
40	2.50×10^{-01}	7.11×10^{-15}	0.00×10^{00}	2.77×10^{-02}	81	5.00×10^{-01}	8.67×10^{-19}	122	0.00×10^{00}	2.55×10^{-05}
41	7.50×10^{-01}	0.00×10^{00}	0.00×10^{00}	2.99×10^{-02}	82	0.00×10^{00}	8.67×10^{-19}	123	0.00×10^{00}	2.17×10^{-19}
								124	4.71×10^{-01}	0.00×10^{00}
								125	1.78×10^{-15}	0.00×10^{00}
								126	5.00×10^{-02}	6.52×10^{-06}
								127	0.00×10^{00}	0.00×10^{00}
								128	0.00×10^{00}	0.00×10^{00}
								129	0.00×10^{00}	0.00×10^{00}
								130	1.78×10^{-15}	0.00×10^{00}
								131	0.00×10^{00}	0.00×10^{00}
								132	5.00×10^{-01}	0.00×10^{00}
								133	0.00×10^{00}	0.00×10^{00}
								134		1.08×10^{-19}
								135		0.00×10^{00}
								136		0.00×10^{00}
								137		0.00×10^{00}

References

1. Müller, G. Review: The Czochralski Method—where we are 90 years after Jan Czochralski's invention. *Cryst. Res. Technol.* **2007**, *42*, 1150–1161. [[CrossRef](#)]
2. Rudolph, P.; Nishinga, T. *Handbook of Crystal Growth: Bulk Crystal Growth*; Elsevier: Amsterdam, The Netherlands, 2014; Volume 2, pp. 389–397.
3. Friedrich, J.; von Ammon, W.; Müller, G. Czochralski Growth of Silicon Crystals. In *Handbook of Crystal Growth: Bulk Crystal Growth*; Rudolph, P., Ed.; Elsevier Science: Amsterdam, The Netherlands, 2014; pp. 47–61.
4. Su, W.; Zuo, R.; Mazaev, K.; Kalaev, V. Optimization of crystal growth by changes of flow guide, radiation shield and sidewall insulation in Cz Si furnace. *J. Cryst. Growth* **2010**, *312*, 495–501. [[CrossRef](#)]
5. Noghabi, O.A.; M'Hamdi, M.; Jomâa, M. Sensitivity analyses of furnace material properties in the Czochralski crystal. *Meas. Sci. Technol.* **2013**, *24*, 015601. [[CrossRef](#)]
6. Dornberger, E.; Tomzig, E.; Seidl, A.; Schmitt, S.; Leister, H.-J.; Schmitt, C.; Müller, G. Thermal simulation of the Czochralski silicon growth process by three different models and comparison with experimental results. *J. Cryst. Growth* **1997**, *180*, 461–467. [[CrossRef](#)]
7. Tsukada, T.; Imaishi, N.; Hozawa, M. Effect of a radiation shield on melt crystal interface shape and pull rate of silicon CZ puller. *J. Chem. Eng. Jpn.* **1988**, *21*, 381–387. [[CrossRef](#)]
8. Mosel, F.; Denisov, A.V.; Klipp, B.; Sennova, N.; Kranert, C.; Jung, T.; Trempa, M.; Reimann, C.; Friedrich, J. Limitations of the growth rate of silicon mono ingots grown by the Czochralski technique. *Proc. EU PVSEC* **2020**, 468–473.
9. Ding, J.; Liu, L. Real-time prediction of crystal/melt interface shape during Czochralski crystal growth. *Cryst. Eng. Comm.* **2018**, *20*, 6925–6931. [[CrossRef](#)]
10. Van den Bogaert, N.; Dupret, F. Dynamic global simulation of the Czochralski process, II. Analysis of the growth of a germanium crystal. *J. Cryst. Growth* **1997**, *171*, 77–93. [[CrossRef](#)]
11. Böttcher, K.; Rudolph, P.; Neubert, M.; Kurz, M.; Pusztai, A.; Müller, G. Global temperature field simulation of the vapour pressure controlled Czochralski (VCz) growth of 3"–4" gallium arsenide crystals. *J. Cryst. Growth* **1999**, *198*, 349–354. [[CrossRef](#)]
12. Derby, J.J.; Atherton, L.J.; Gresho, P.M. An integrated process model for the growth of oxide crystals by the Czochralski method. *J. Cryst. Growth* **1989**, *97*, 792–826. [[CrossRef](#)]
13. Hur, M.J.; Han, X.F.; Song, D.S.; Kim, T.H.; Lee, N.J.; Jeong, Y.J.; Yi, K.W. The influence of crucible and crystal rotation on the sapphire single crystal growth interface shape in a resistance heated Czochralski system. *J. Cryst. Growth* **2014**, *385*, 22–27. [[CrossRef](#)]
14. Fühner, T.; Jung, T. Use of genetic algorithms for the development and optimization of crystal growth processes. *J. Cryst. Growth* **2004**, *266*, 229–238. [[CrossRef](#)]
15. Smirnova, O.V.; Durnev, N.V.; Shandrakova, K.E.; Mizitov, E.L.; Soklakov, V.D. Optimization of furnace design and growth parameters for Si Cz growth, using numerical simulation. *J. Cryst. Growth* **2008**, *310*, 2185–2191. [[CrossRef](#)]
16. Müller, G.; Fischer, B. *Optimization of Melt Growth Processes by Experimental Analysis and Computer Modelling*; Sato, K., Furukawa, Y., Nakajima, K., Ohachi, T., Eds.; Proceedings of the ISSCG 11; Elsevier: Amsterdam, The Netherlands, 2001; pp. 167–190.
17. Huang, L.Y.; Lee, P.C.; Hsieh, C.K.; Hsu, W.C.; Lan, C.W. On the hot-zone design of Czochralski silicon growth for photovoltaic applications. *J. Cryst. Growth* **2004**, *261*, 433–443. [[CrossRef](#)]
18. Dornberger, E.; von Ammon, W.; Van den Bogaert, N.; Dupret, F. Transient computer simulation of a CZ crystal growth process. *J. Cryst. Growth* **1996**, *166*, 452–457. [[CrossRef](#)]
19. Noghabi, O.A.; M'Hamdi, M.; Jomâa, M. Effect of crystal and crucible rotations on the interface shape of Czochralski grown silicon single crystals. *J. Cryst. Growth* **2011**, *318*, 173–177. [[CrossRef](#)]
20. Rea, S.N. Czochralski silicon pull rate limits. *J. Cryst. Growth* **1981**, *54*, 267–274. [[CrossRef](#)]
21. Friedrich, J.; Jung, T.; Trempa, M.; Reimann, C.; Denisov, A.; Muehe, A. Considerations on the limitations of the growth rate during pulling of silicon crystals by the Czochralski technique for PV applications. *J. Cryst. Growth* **2019**, *524*, 125168. [[CrossRef](#)]
22. Kakimoto, K.; Yi, K.-W.; Eguchi, M. Oxygen transfer during single silicon crystal growth in Czochralski system with vertical magnetic fields. *J. Cryst. Growth* **1996**, *163*, 238–242. [[CrossRef](#)]
23. Kakimoto, K.; Eguchi, M.; Ozoe, H. Use of an inhomogenous magnetic field for silicon crystal growth. *J. Cryst. Growth* **1997**, *180*, 442–449. [[CrossRef](#)]
24. Liu, L.; Kakimoto, K. Partly three-dimensional global modeling of a silicon Czochralski furnace. II. Model application: Analysis of a silicon Czochralski furnace in a transverse magnetic field. *Int. J. Heat Mass Transf.* **2005**, *48*, 4492–4497. [[CrossRef](#)]
25. Smirnov, A.D.; Kalaev, V.V. Development of oxygen transport model in Czochralski growth of silicon crystals. *J. Cryst. Growth* **2008**, *310*, 2970–2976. [[CrossRef](#)]
26. Gao, B.; Kakimoto, K. Global simulation of coupled carbon and oxygen transport in a Czochralski furnace for silicon crystal growth. *J. Cryst. Growth* **2010**, *312*, 2972–2976. [[CrossRef](#)]
27. Dropka, N.; Holena, M. Application of Artificial Neural Networks in Crystal Growth of Electronic and Opto-Electronic Materials. *Crystals* **2020**, *10*, 663. [[CrossRef](#)]
28. Curtolo, D.C.; Friedrich, S.; Friedrich, B. High Purity Germanium, a Review on Principle Theories and Technical Production Methodologies. *J. Cryst. Process Technol.* **2017**, *7*, 65–84. [[CrossRef](#)]

29. Depuydt, B.; Theuwis, A.; Romandic, I. Germanium: From the first application of Czochralski crystal growth to large diameter dislocation-free wafers. *Mater. Sci. Semicond. Process.* **2006**, *9*, 437–443. [[CrossRef](#)]
30. Abrosimov, N.; Czupalla, M.; Dropka, N.; Fischer, J.; Gybin, A.; Irmscher, K.; Janicskó-Csáthy, J.; Juda, U.; Kayser, S.; Miller, W.; et al. Technology Development of High Purity Germanium Crystals for Radiation Detectors. *J. Cryst. Growth* **2020**, *532*, 125396. [[CrossRef](#)]
31. Sumathi, R.R.; Abrosimov, N.; Gradwohl, K.-P.; Czupalla, M.; Fischer, J. Growth of heavily-doped Germanium single crystals for mid-Infrared applications. *J. Cryst. Growth* **2020**, *535*, 125490. [[CrossRef](#)]
32. Yu, W.; Zhu, C.; Tsunooka, Y.; Huang, W.; Dang, Y.; Kutsukake, K.; Harada, S.; Tagawa, M.; Ujihara, T. Geometrical design of a crystal growth system guided by a machine learning algorithm. *Cryst. Eng. Comm.* **2021**, *23*, 2695–2702. [[CrossRef](#)]
33. Kutsukake, K.; Nagai, Y.; Banba, H. Virtual experiments of Czochralski growth of silicon using machine learning: Influence of processing parameters on interstitial oxygen concentration. *J. Cryst. Growth* **2022**, *584*, 126580. [[CrossRef](#)]
34. Kutsukake, K.; Nagai, Y.; Horikawa, T.; Banba, H. Real-time prediction of interstitial oxygen concentration in Czochralski silicon using machine learning. *Appl. Phys. Express.* **2020**, *13*, 125502. [[CrossRef](#)]
35. Qi, X.; Ma, W.; Dang, Y.; Su, W.; Liu, L. Optimization of the melt/crystal interface shape and oxygen concentration during the Czochralski silicon crystal growth process using an artificial neural network and a genetic algorithm. *J. Cryst. Growth* **2020**, *548*, 125828. [[CrossRef](#)]
36. Asadian, M.; Seyedein, S.H.; Aboutalebi, M.R.; Maroosi, A. Optimization of the parameters affecting the shape and position of crystal-melt interface in YAG single crystal growth. *J. Cryst. Growth* **2009**, *311*, 342–348. [[CrossRef](#)]
37. Takehara, Y.; Sekimoto, A.; Okano, Y.; Ujihara, T.; Dost, S. Explainable machine learning for the analysis of transport phenomena in top-seeded solution growth of SiC single crystal. *J. Therm. Sci. Technol.* **2021**, *16*, 20–00269. [[CrossRef](#)]
38. Shalev-Shwartz, S.; Ben-David, S. Decision Trees. In *Understanding Machine Learning*; Cambridge University Press: Cambridge, UK, 2014.
39. Breiman, L.; Friedman, J.; Olshen, R.; Stone, C. *Classification and Regression Trees*; CRC Press: Boca Raton, FL, USA, 1984.
40. Dropka, N.; Böttcher, K.; Holena, M. Development and optimization of VGF-GaAs crystal growth process using data mining and machine learning techniques. *Crystals* **2021**, *11*, 1218. [[CrossRef](#)]
41. Kakimoto, K.; Gao, B. Fluid Dynamics: Modeling and Analysis. In *Handbook of Crystal Growth*; Rudolph, P., Ed.; Elsevier: Amsterdam, The Netherlands, 2015; pp. 845–870.
42. Montgomery, D. *Design and Analysis of Experiments*, 8th ed.; John Wiley & Sons, Inc.: Hoboken, NJ, USA, 2013.
43. Jiptner, K.; Gao, B.; Harada, H.; Miyamura, Y.; Fukuzawa, M.; Kakimoto, K.; Sekiguchi, T. Thermal stress induced dislocation distribution in directional solidification of Si for PV application. *J. Cryst. Growth* **2014**, *408*, 19–24. [[CrossRef](#)]
44. Voronkov, V.V. The mechanism of swirl defects formation in silicon. *J. Cryst. Growth* **1982**, *59*, 625–643. [[CrossRef](#)]
45. Dornberger, E.; Graef, D.; Suhren, M.; Lambert, U.; Wagner, P.; Dupret, F.; von Ammon, W. Influence of boron concentration on the oxidation-induced stacking fault ring in Czochralski silicon crystals. *J. Cryst. Growth* **1997**, *180*, 343–352. [[CrossRef](#)]
46. Wang, G.; Guan, Y.; Mei, H.; Mei, D.; Yang, G.; Govani, J.; Khizar, M. Dislocation Density Control in High-Purity Germanium Crystal Growth. *J. Cryst. Growth* **2014**, *393*, 54–58. [[CrossRef](#)]
47. Vanhellemont, J.; Nakamura, K.; Kamiyama, E.; Sueoka, K. Control of Intrinsic Point Defects in Single-Crystal Si and Ge Growth from a Melt. In *Defects and Impurities in Silicon Materials. Lecture Notes in Physics*; Yoshida, Y., Langouche, G., Eds.; Springer: Minato-Ku, Tokyo, 2015.
48. Vanhellemont, J.; Kamiyama, E.; Nakamura, K.; Spiewak, P.; Sueoka, K. Impacts of thermal stress and doping on intrinsic point defect properties and clustering during single crystal silicon and germanium growth from a melt. *J. Cryst. Growth* **2017**, *474*, 96–103. [[CrossRef](#)]
49. Dang, Y.; Liu, L.; Li, Z. Optimization of the controlling recipe in quasi-single crystalline silicon growth using artificial neural network and genetic algorithm. *J. Cryst. Growth* **2019**, *522*, 195–203. [[CrossRef](#)]
50. Box, G.E.P.; Hunter, W.G.; Hunter, J.S. *Statistics for Experimenters: An Introduction to Design, Data Analysis and Model Building*; Wiley: New York, NY, USA, 1978.